MECHANICAL PROPERTIES, CORROSION BEHAVIOR AND BIOCOMPATIBILITY OF NICKEL-FREE AUSTENITIC STAINLESS STEEL (HNS)

3.1. Introduction

A nickel-free grade of austenitic stainless steel (HNS) was procured from M/s Jindal Stainless Ltd., Hisar, India. This steel was developed by Jindal Stainless Ltd., Hisar. It had been well characterized and also used for structural applications, but not from the point of view of biomedical applications. This chapter presents the microstructural characterization, electrochemical corrosion resistance in Ringer's solution, biocompatibility, tensile and fatigue properties of the HNS and their comparison with that of 316L. Tensile strength of the HNS is found higher than 316L, however, its pitting potential and endurance limit at 10^7 cycles in air were lower than 316L. The *in vitro* and *in vivo* studies revealed acceptable biocompatibility of the HNS.

3.2. Microstructure Characterization of the HNS and 316L

The optical micrographs of the HNS and 316L are shown in **Fig. 3.1**. They consist of equiaxed austenite grains with few annealing twins. The mean intercept length of the HNS and 316L was 36 ± 6 μm and 29 ± 4 μm, respectively. The microstructures were also characterized according to the ASTM E-407-07 (2015) standard and there was no carbide precipitation at the grain boundaries of the both HNS and 316L. The presence of delta ferrite was insignificant in the HNS, whereas it was ~ 3.5 % in the 316L according to the ASTM E-562 (2011).

The inclusion rating of the HNS is given in **Table 3.1**, it was found within the limit as per the ISO 5832-1 standard. The X-ray diffraction patterns (with Cu-Kα radiation) of

the HNS and 316L are shown in **Fig 3.2**. Only the peaks of austenite were observed for both the stainless steels.
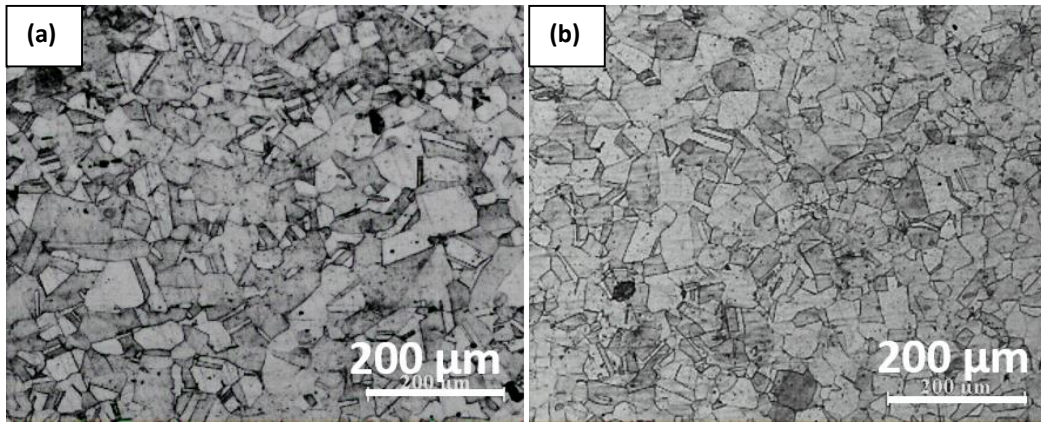
Fig. 3.1. Optical micrographs showing microstructure of the (a) HNS and (b) 316L austenitic stainless steels.

Table 3.1. Inclusion rating of the HNS austenitic stainless steel.

| Types of inclusion	A		B		C		D	
	Thin	**Heavy**	**Thin**	**Heavy**	**Thin**	**Heavy**	**Thin**	**Heavy**
Determined values	Nil	Nil	1	Nil	2	Nil	1	Nil
Permissible limit (ISO 5832-1)	1.5	1	1.5	1	1.5	1	1.5	1
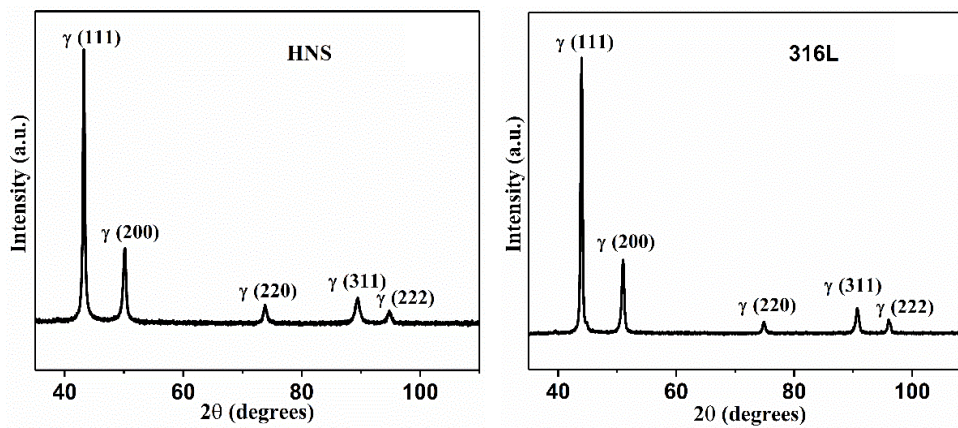
Fig. 3.2. XRD patterns of the austenitic stainless steels: (a) HNS and (b) 316L.

3.3. Comparison of Corrosion Behavior of the HNS and 316L

Corrosion tests were performed to evaluate pitting and intergranular corrosion resistance of the HNS and 316L austenitic stainless steels. Step structure was observed in the both HNS as well as 316L steels when etched with 10 % oxalic acid and 10% Ammonium persulphate, respectively, according to the ASTM A-262 practice A. Fissures were absent after 15 h of boiling in copper-copper sulphate, 16% sulphuric acid solution. The microstructures of the HNS and 316L were found free from intergranular corrosion and grain dropping, according to the ASTM A-262-15 practice E. Corrosion rate of 48.52 g/m^2 and 368.88 g/m^2 for the HNS and 316L stainless steels was observed, respectively; in 6% FeCl$_3$ solution according to the ASTM G 48-11 Method-A. The maximum depth of attack was found to be 0.12 mm and 0.05 mm for the HNS and 316L, respectively, at 22ºC for 24 h of exposure, according to the ASTM G 48-11 Method-D.

Electrochemical corrosion resistance was studied using potentiodynamic polarization. **Fig 3.3** shows the potentiodynamic polarization curves of the HNS and 316L. The various corrosion data were estimated from the potentiodynamic curves and these are tabulated in **Table 3.2**. The 316L has a higher breakdown potential than that of the HNS. However, the critical current density of the HNS is lower than that of 316L (**Table 3.2**).
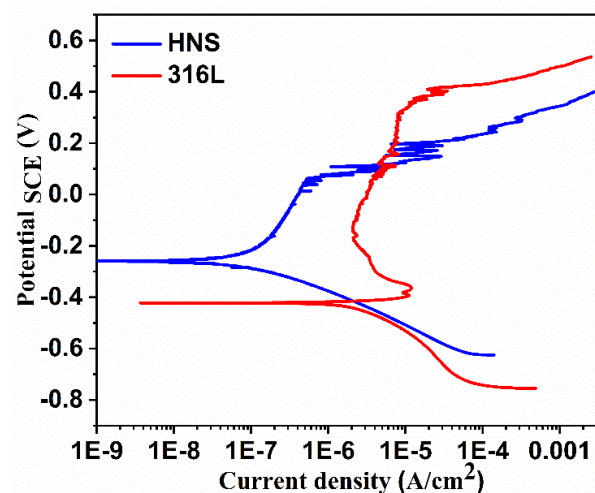
Fig. 3.3. Potentiodynamic polarization curves of the HNS and 316L austenitic stainless steels.

**Table 3.2.** Corrosion data of the HNS and 316L austenitic stainless steels.

Material	Corrosion potential, E_{corr} (mV$_{SCE}$)	Breakdown potential (mV)	Critical current density, i_{cr} (µA/cm^2)
316L	-421	316	11.8
HNS	-260	196	0.11

3.4. Comparison of Mechanical Properties of the HNS and 316L

Various mechanical properties of the HNS were determined by conducting tensile tests, Vickers hardness test, strain-controlled low cycle fatigue and stress-controlled high cycle fatigue tests, and the results were compared with that of the 316L stainless steel.

3.4.1. Tensile Properties and Hardness

Engineering stress-strain plots of the HNS and 316L are shown in **Fig. 3.4.** The various parameters were evaluated and are presented in **Table 3.3**.
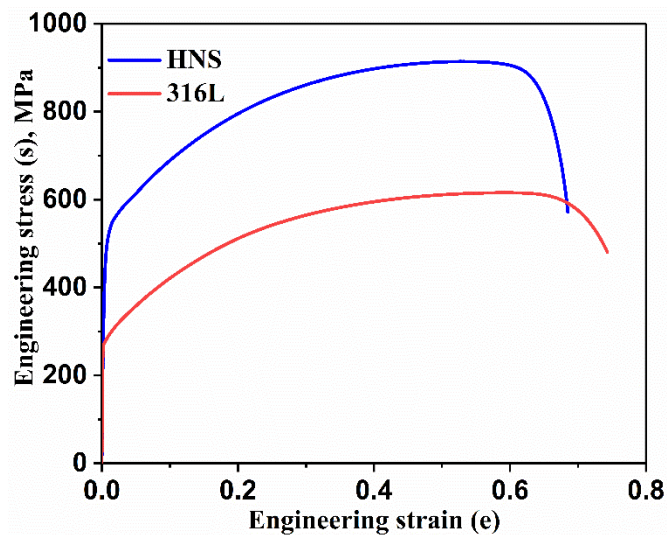
Fig. 3.4. Comparison of engineering stress-strain curves of the HNS and 316L austenitic stainless steels.

Table 3.3. Tensile properties of the HNS and 316L austenitic stainless steels.

Stainless steel	Yield strength (MPa)	Ultimate tensile strength (MPa)	Uniform strain (%)	Total strain (%)	UTS/YS
HNS	525	914	52	68	1.74
316L	279	616	58	74	2.21

It may be observed that the HNS has higher yield strength (YS) and ultimate tensile strength (UTS), whereas its ductility is marginally lower than that of the 316L. However, it has a sufficiently high uniform strain of 52%. The Vickers hardness of the HNS and 316L was found 307 ± 4 Hv and 140 ± 6 Hv, respectively.

3.4.2. Low Cycle Fatigue Behavior

The HNS and 316L samples were tested for low cycle fatigue in total strain-controlled mode at different total strain amplitudes ($\pm\Delta\varepsilon_t/2$) and their cyclic stress response with increasing cycle was recorded. Also, the LCF life and hardening/softening behavior of the HNS was compared with that of the 316L. **Fig. 3.5** shows the variation of cyclic stress amplitude ($\Delta\sigma/2$) of the HNS and 316L.
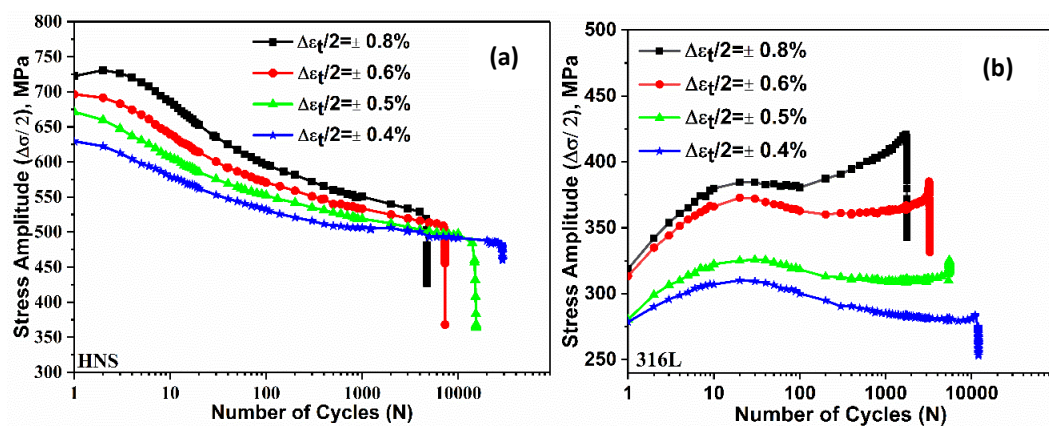
Fig. 3.5. Cyclic stress response curves of the austenitic stainless steels: (a) HNS and (b) 316L.

There is a notable difference in the cyclic stress behavior of both the steels. There was a prominent cyclic softening in the HNS, whereas there was initial cyclic hardening in the 316L. The cyclic hardening/softening behavior of both the steels was dependent on the $\pm\Delta\varepsilon_t/2$. It is evident from **Fig. 3.5a** that in the HNS, there is a gradual cyclic softening from the beginning, at $\Delta\varepsilon_t/2$ ranging from $\pm\ 0.40\%$ to $\pm\ 0.60\%$, whereas at $\Delta\varepsilon_t/2 = \pm\ 0.80\%$, there is marginal hardening during the initial 2-3 cycles, and is followed by softening.

The cyclic stress response of the 316L is shown in **Fig. 3.5b**. There was primary cyclic hardening during the initial few cycles at all the $\Delta\varepsilon_t/2$. At lower $\Delta\varepsilon_t/2$ of $\pm\ 0.40\%$, primary cyclic hardening was observed for the initial 30 cycles and thereafter cyclic softening was recorded up to the failure. At the intermediate $\Delta\varepsilon_t/2$ of $\pm\ 0.50\%$ and $\pm\ 0.60\%$, primary cyclic hardening was recorded for the initial 30 cycles and then cyclic softening for most of the fatigue life and a mild secondary hardening was seen in the last. There is primary cyclic hardening during the initial 20 cycles at $\Delta\varepsilon_t/2$ of $\pm\ 0.80\%$, after that, there was cyclic softening till 100 cycles, followed by a prominent secondary cyclic hardening at the end.

The data of the LCF tests of the HNS and 316L samples are presented in **Table 3.4**. The number of cycles endured before failure (N_f) is progressively increased with decreasing $\Delta\varepsilon_t/2$ for both the HNS and 316L. The fatigue life of the HNS is $\sim$ 2 times that of the 316L at a given $\Delta\varepsilon_t/2$. The LCF life is analyzed using the Coffin-Manson relationship, shown below in **Eq. 3.1** [171,172].

$$\frac{\Delta\varepsilon_t}{2} = \frac{\Delta\varepsilon_e}{2} + \frac{\Delta\varepsilon_p}{2} = \frac{\sigma'_f}{E}(2N_f)^b + \varepsilon'_f(2N_f)^c \tag{3.1}$$

In **Eq. 3.1**, $\Delta\varepsilon_t/2$, $\Delta\varepsilon_e/2$, $\Delta\varepsilon_p/2$, σ'_f, b, ε'_f, c, E and N_f are total strain amplitude, elastic strain amplitude, plastic strain amplitude, fatigue strength coefficient, fatigue strength

exponent, fatigue ductility coefficient, fatigue ductility exponent, elastic modulus and fatigue life, respectively.

Table 3.4. LCF data of the HNS and 316L austenitic stainless steels.

Stainless steel	Total strain amplitude ($\pm \Delta\varepsilon_t/2$) (%)	Elastic strain amplitude ($\pm \Delta\varepsilon_e/2$) (%) at $N_f/2$	Plastic strain amplitude ($\pm \Delta\varepsilon_p/2$) (%) at $N_f/2$	Fatigue life (N_f) cycles
HNS	0.40	0.26	0.14	28927
	0.50	0.27	0.23	15389
	0.60	0.27	0.33	7330
	0.80	0.28	0.52	4760
316L	0.40	0.14	0.26	12049
	0.50	0.17	0.33	5551
	0.60	0.18	0.42	3268
	0.80	0.22	0.58	1779

Note: N_f: Fatigue life, $N_f/2$: Half-fatigue life

The dependence of the number of reversals to failure ($2N_f$) on $\Delta\varepsilon_p/2$ for the HNS and 316L is shown in **Fig. 3.6**.
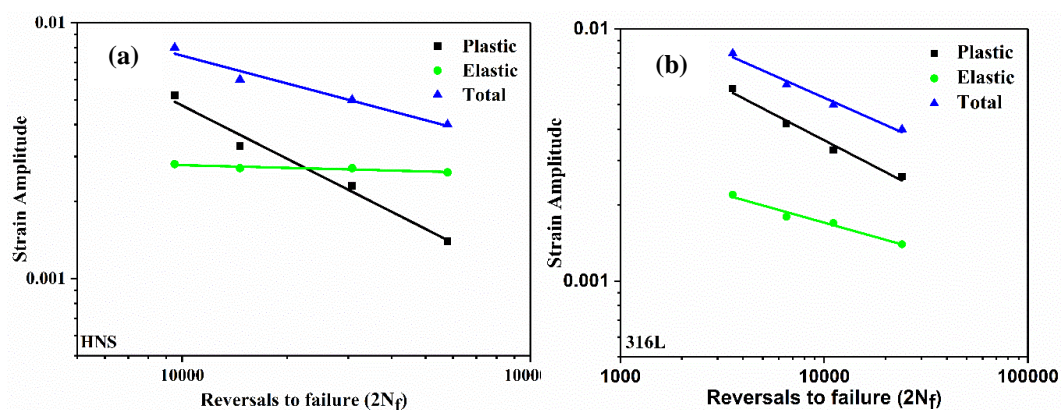
Fig. 3.6. Variation of the number of reversals to failure ($2N_f$) with strain amplitude for the austenitic stainless steels: (a) HNS and (b) 316L.

The parameters characterizing HCF (σ'_f & b) and LCF (ε'_f & c) were evaluated from the plots of $\Delta\varepsilon_e/2$ vs $2N_f$ and $\Delta\varepsilon_p/2$ vs $2N_f$ and their values are presented in **Table 3.5**. The HNS has higher ε'_f but lower σ'_f as compared to 316L.

Table 3.5. Fatigue parameters based on strain-life relationships.

Stainless steel	σ'_f (MPa)	b	ε'_f	c
HNS	727	-0.035	2.728	-0.689
316L	2605	-0.226	0.171	-0.419

3.4.3. High Cycle Fatigue Behavior in Air

The high cycle fatigue behavior of the HNS was studied and compared with that of the 316L. The fatigue life data at various maximum stresses are presented in **Table 3.6**.

Table 3.6. Comparison of high cycle fatigue life of the HNS and 316L austenitic stainless steels at various maximum stresses.

Maximum stress, MPa	Fatigue life (N_f)	
	HNS	316L
550	486013	117046
538	1049450	360417
	1073080	
525	2739134	5093733
	2470231	
513	-	NF
500	4797074	NF
	4292637	
485	8643700	-
475	NF	-

Note: NF: not failed at 10^7 cycles

Fig. 3.7 shows the stress-number of cycles (S-N) curves of the HNS and 316L austenitic stainless steels tested in air at a stress ratio (R) of 0.1. The stress shown along the y-axis

is maximum stress, and the number of cycles to failure (N_f) is shown along the x-axis on a logarithmic scale. N_f was found to increase with decrease in the stress for both the steels. The maximum stress corresponding to endurance limit at 10^7 cycles for the HNS and 316L was observed as 475 MPa and 513 MPa, respectively. Both the S-N curves intersect, which indicates that the HNS has higher fatigue life at higher maximum stresses ($\geq$ 538 MPa), whereas at lower stresses ($\leq$ 525 MPa), HNS has comparatively lower fatigue life than that of the 316L.
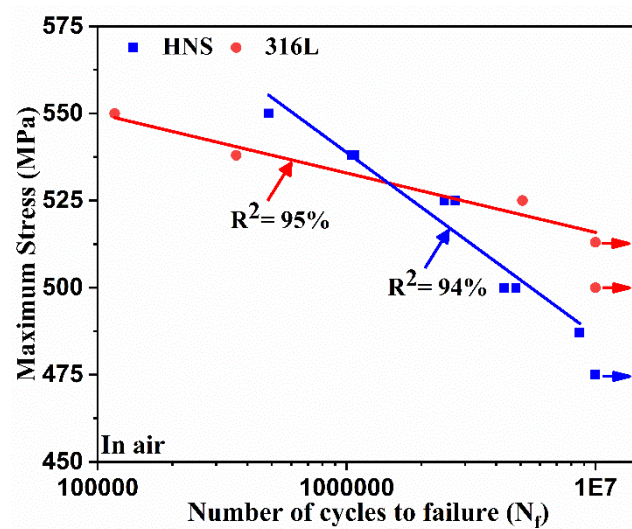

Fig. 3.7. Comparison of high cycle fatigue behavior of the HNS and 316L austenitic stainless steels in air, at stress ratio of 0.1.

3.5. Biocompatibility of HNS

The biocompatibility of HNS was studied both *in vitro* and *in vivo*. *In vitro* cell culture and proliferation experiments were conducted with MG-63 human bone osteosarcoma cells. The results are compared with that of 316L. The *in vivo* animal (implantation) test of HNS was also performed to evaluate the biological response of tissues after implantation.

**3.5.1. *In vitro* Cell Culture and Proliferation**

The fluorescent images of the MG-63 cells on the various samples are shown in **Fig. 3.8**.
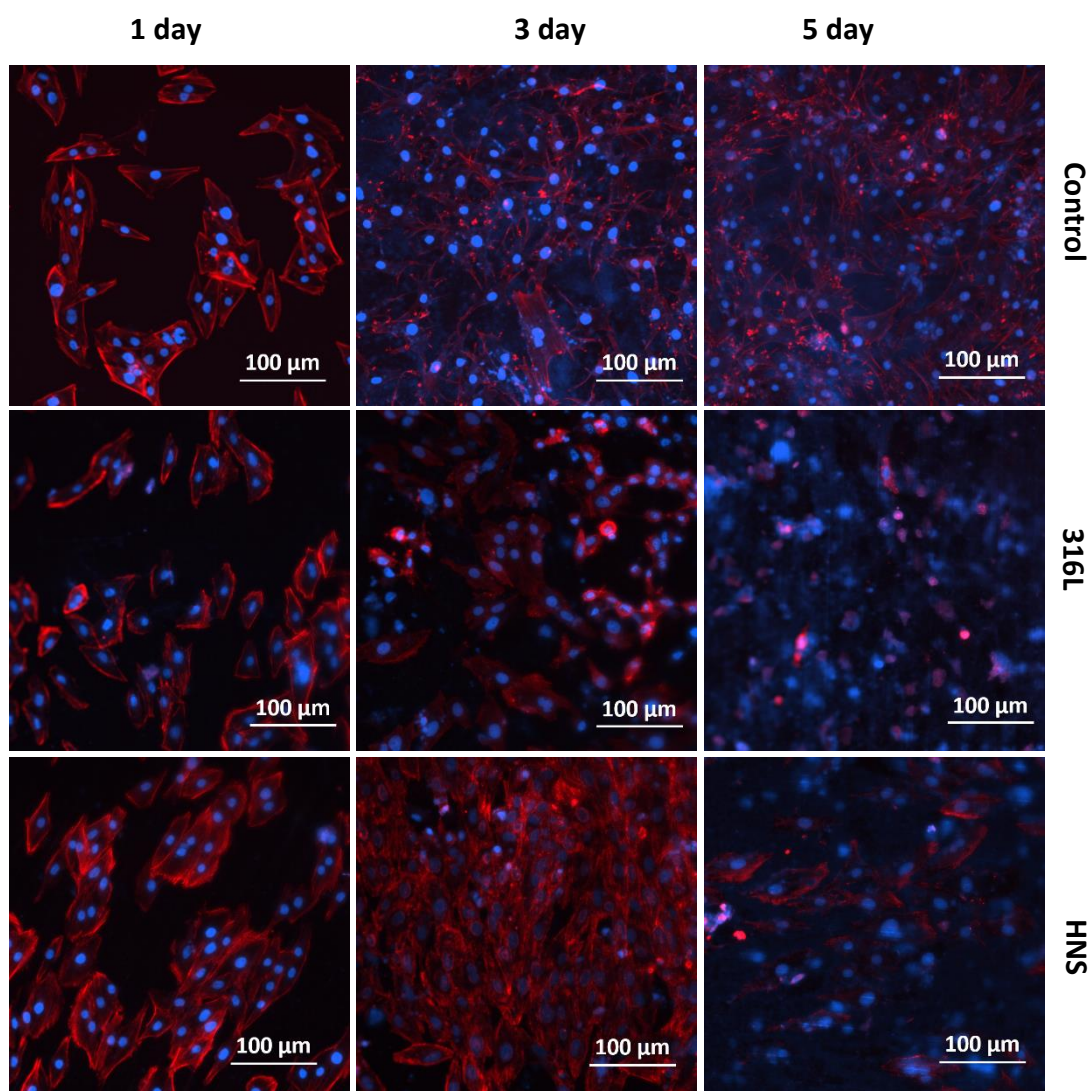
Fig. 3.8. Panel representing the fluorescent cell culture images of the MG-63 human bone osteosarcoma cells on the various steel samples; after 1 day, 3 days and 5 days of incubation. Blue color: nuclei staining; red color: actin cytoskeleton filament staining.

There is an enhancement in the cell coverage with increase in culture time for all the samples, showing a gradual cellular growth over time. Cells on surfaces of both the steels, following 1 day of culture are found scattered and fully spread as well as the cell coverage on both the stainless steels is noted almost similar. However, after 3 days of cell culture, the HNS showed significantly higher cell coverage and spreading compared with that of the 316L. After 5 days of exposure, it is very difficult to differentiate the cell culture, as in both cases, there was clustering of cell nuclei.

The cell proliferation behavior of MG-63 cells on 316L and HNS samples was analyzed using MTT assay. **Fig. 3.9** shows the histograms of the cell proliferation after incubation of 1, 3 and 5 days.
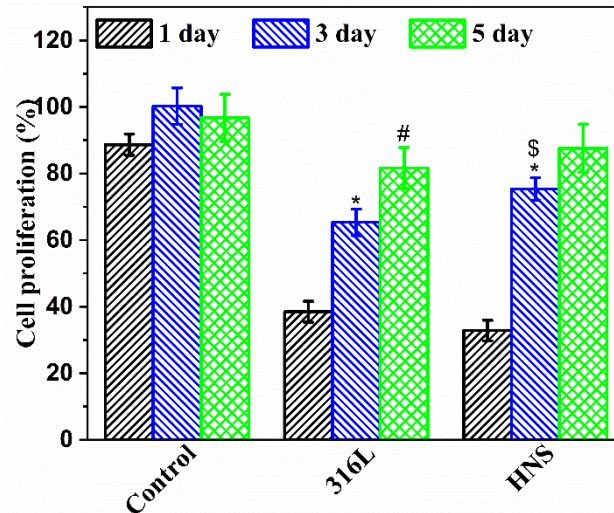

Fig. 3.9. Histograms representing comparison of the MG-63 cell proliferation on the 316L and HNS austenitic stainless steels; after 1, 3 and 5 days of incubation by MTT assay. In this experiment, absorbance of control for the 5th day culture was taken as reference for all the samples. *p ≤ 0.05 with respect to 1 day of corresponding group. $^#$p ≤ 0.05 with respect to 3 days of corresponding group. $^$$p ≤ 0.05 with respect to 3 days of 316L.

There is gradual increase in the mean percent cell proliferation for both the steels with the duration of incubation**.** There is a significant difference at the level of 0.05 between different time points. The cell proliferation for the HNS sample was comparable to that of the 316L, which is commonly used for biomedical applications. However, a statistically significant difference in the cell proliferation of HNS and 316L, was observed at the level of 0.05 after 3 days of culture.

3.5.2. In vivo/Animal Study

To study the *in vivo* behavior of HNS, fracture was created in the femur of rabbits and the fracture was fixed with the HNS wire. It was tested histologically and

radiographically for gross examination. The representative radiographs of the group1 (sacrificed after three weeks) at post-operation day 1 and follow-up at 3 weeks are shown in **Fig. 3.10**.
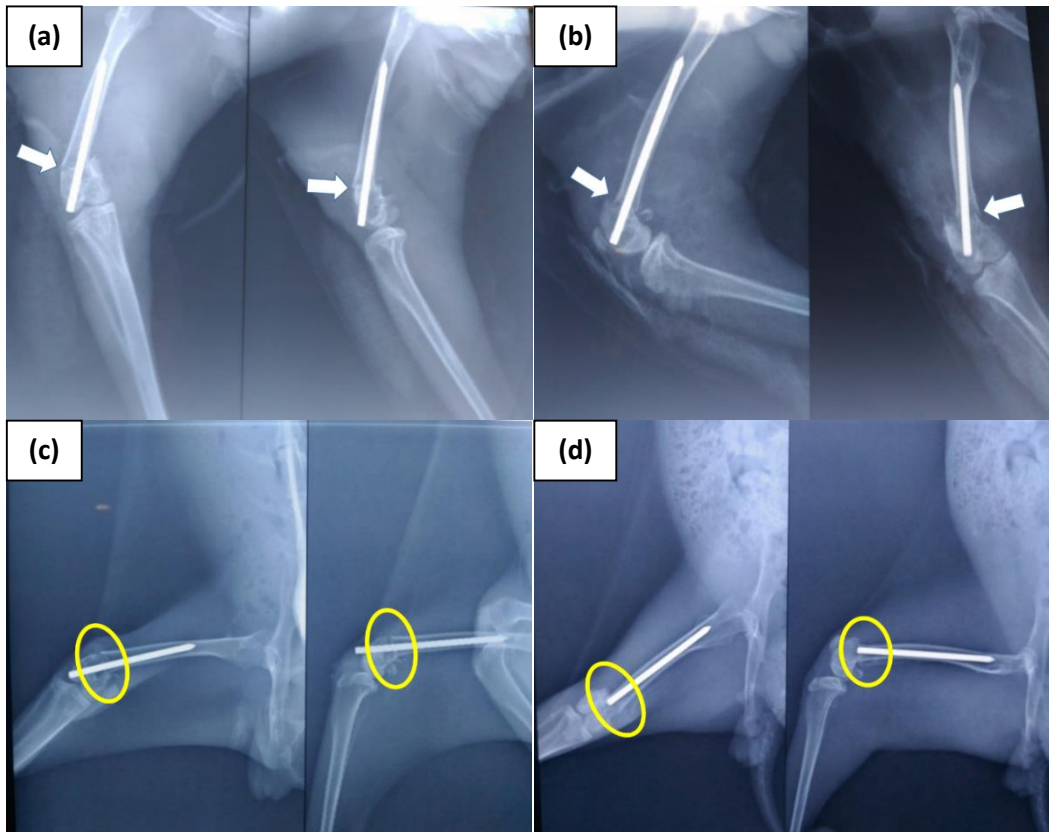

Fig. 3.10. (a, b) Post operation day 1 radiographs of group 1, and (c, d) 3 weeks follow up radiographs of the respective cases of group 1. Arrows indicate the fracture sites and the encircled regions show the union of fracture after 3 weeks.

The radiographs of group 2 (sacrificed after six weeks) are shown in **Fig. 3.11.** Radiographically, both the groups showed sign of union. However, group 2 (6-week group) showed an appreciable increase in the union (**Fig. 3.11c**) indicating that the created fracture is proceeding to union with time. On gross examinations, callus was seen in all the cases, as shown in **Fig. 3.12**. The post-operative skin condition at three weeks and six weeks was normal and there was no sign of inflammation and allergic reaction.
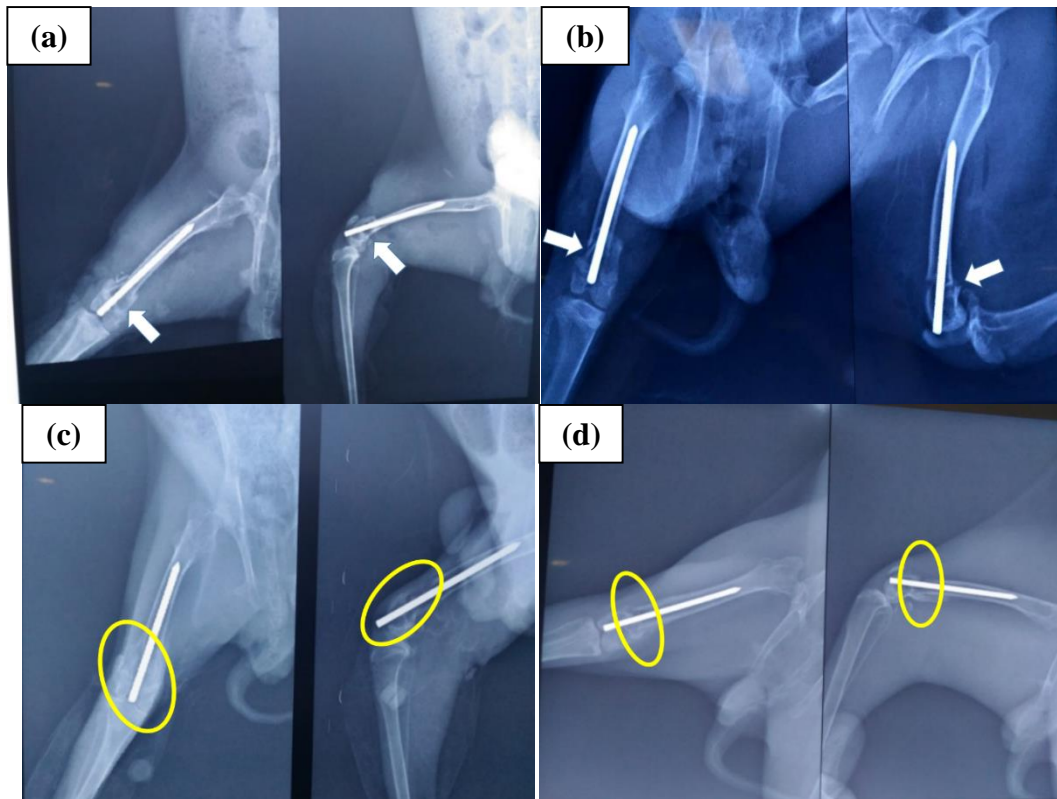
Fig. 3.11. (a, b) Post operation day 1 radiographs of group 2, and (c, d) 6 weeks follow up radiographs of the respective cases of group 2. Arrows indicate the fracture sites and the encircled regions show the union of fracture after 6 weeks.
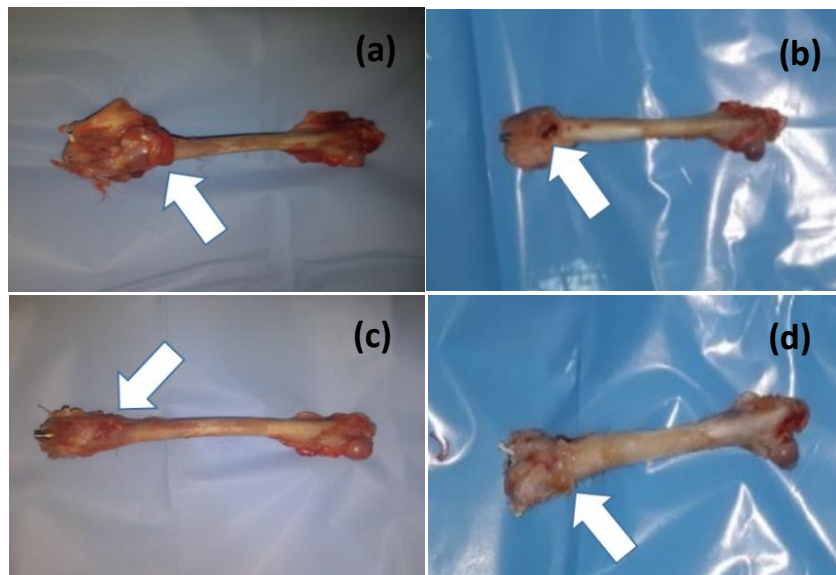
Fig. 3.12. Post operation - after harvesting femur: (a, b) at 3 weeks (group 1); and (c, d) at 6 weeks (group 2). Arrows show the callus.

3.5.2.1. Histopathology

Bone biopsy

At three weeks, sections revealed viable bony trabeculae with marrow spaces. The proliferation of fibroblast, irregular bony trabeculae and lobules of cartilage with chondroblasts were seen; whereas, at six weeks, sections revealed thickened mineralized bony trabeculae with marrow spaces. In one case, an occasional lobule of cartilage was noted.

Soft tissue biopsy

At three weeks, sections revealed organizing granulation tissue with moderate inflammation. In one case, few scattered foreign body granules were seen. At six weeks, sections showed scar tissue with mild inflammatory infiltrates and fibrosis.

3.6. Discussion

Stainless steel for medical applications should be cost-effective and possess sufficiently high mechanical properties like strength, fatigue resistance, chemical resistance in body fluid environment and have adequate biocompatibility. It should be non-magnetic. The objective of the present study was to characterize the HNS steel for biomedical applications. This HNS steel was studied in detail for all of its essential requirements to be used as a biomedical material.

3.6.1. Microstructure and Corrosion Resistance

The HNS steel was found austenitic with negligible delta ferrite. The microstructure of stainless steels are highly dependent on their elemental constituents. The HNS was found to be free from ferrite phase which may be due to high content of manganese and absence of molybdenum. Manganese and molybdenum increase the solubility of nitrogen in austenitic stainless steel; however, molybdenum promotes ferrite formation [65]. The

inclusions in the HNS were found as per the requirement of ISO 5832-1 standard. The grain boundaries were found free from precipitates, which shows that the HNS has not been sensitized. It is one of the essential requirements of a material to be used for biomedical applications. The carbides and nitrides precipitate in high nitrogen austenitic stainless steels; however, the high amount of manganese increases solubility limit of nitrogen in austenites and it was found in the solution state.

The theoretical corrosion resistance of materials is estimated by PREN and MARC values. In general, the PREN number is dependent on the Cr, Mo, Mn and N content of stainless steels. The PREN and MARC values were calculated according to the **Eqs. 1.6 and 1.7** for the HNS and 316L stainless steels and are presented in **Table 3.7**.

Table 3.7. Theoretical PREN and MARC values of the HNS and 316L austenitic stainless steels.

Stainless steel	PREN	MARC
HNS	15.59	21.21
316L	21.70	20.28

PREN values are in agreement with the pitting potential obtained from potentiodynamic polarization tests. The HNS has a lower PREN as compared to 316L and it has lower pitting potential **(Fig. 3.3)**. MARC value of the HNS is more than that of 316L. MARC was correlated with the critical pitting corrosion temperature and critical crevice corrosion temperature, and both were observed to increase with MARC [84]. Both HNS and 316L showed step-like structure when tested according to ASTM A-262 practice A. The HNS has a lower corrosion rate than 316L when tested as per ASTM G-48-11 method-A at constant temperature of 22 °C for 24 hours.

XPS analysis of the passive film formed on high manganese and nitrogen stainless steel in acidic NaCl (0.05 mol/L H_2SO_4 + 0.5 mol/L NaCl) solution shows that it was composed of iron oxides, manganese oxides, Cr_2O_3 and $Cr(OH)_3$. An enrichment of Cr

was also observed due to the preferential dissolution of Fe and Mn into the solution and very limited mobility of Cr in surface films [173]. Therefore, enrichment of chromium and nitrogen in the passive oxide film, and at the metal and passive oxide layer interface enhances the pitting resistance of nitrogen-containing stainless steels. The pitting potential was found lower in high manganese steels than in low manganese steels, regardless of the high nitrogen content [67]. The negative effect of manganese on the local corrosion resistance can be understood.

3.6.2. Mechanical Behavior

The interstitial atoms in the solid solution have a significant impact on the strengthening of stainless steel. Fe-Cr-Mn-based austenitic stainless steels have more potential for solubility of nitrogen than Fe-Cr-Ni-based austenites [51]. Interstitial atoms prefers to occupy the octahedral site in the FCC crystal lattice, whereas they occupy tetrahedral site in BCC lattice. It is due to more volume of octahedral sites than tetrahedral in FCC. The size of nitrogen atom (atomic radius) is smaller than that of the carbon atom. However, there is stronger bonding in Fe-C than in Fe-N and nitrogen causes higher distortion in FCC lattice than carbon [60]. Further, there is a short-range ordering of Cr-N [69,70]. Therefore, HNS has higher strength than that of the 316L due to effective pinning of dislocations by atoms, associated with large lattice distortion due to nitrogen atoms and short-range ordering which hinders the dislocation gliding.

The variation of cyclic stress amplitude, with number of cycles at $\Delta\varepsilon_t/2$ from $\pm 0.40\%$ to $\pm 0.80\%$ in the present investigation for HNS, is similar to that in the earlier study on the HNS [167]. Cyclic softening in HNS in the present study, from the very beginning, is in line with the earlier observation of Shao et al. [104] in the Fe-18Cr-18Mn-0.63N steel up to $\Delta\varepsilon_t/2= \pm 1.0\%$, which was attributed to the disordering of the Cr-N short-range orders. SFE of the nitrogen stabilized stainless steel is low; it was 41 mJ/m^2 for the Fe-15Cr-17Mn-0.8N and 22.8 mJ/m^2 for the Fe-18Cr-10Mn-0.69N [71,72]. Dislocation arrays

form easily due to planar slip and remain localized in specific slip planes in the low stacking fault energy materials, whereas dislocation cell structure forms in the high nitrogen stainless steels, during cyclic softening [104].

The variation of cyclic stress amplitude with number of cycles for 316L is different from that of the HNS (**Fig. 3.5**). A prominent secondary cyclic hardening was recorded with increasing strain amplitude. Hong et al. [174] observed a similar stress response of 316L at RT, tested at 1×10^{-3} /sec constant strain rate. In contrast, continuous softening after initial hardening was observed at all the ranges of strain amplitudes [175]. Lei et al. [176] observed similar stress response for coarse-grained 316L in LCF at 3.6×10^{-2} /sec constant strain rate. There is increase in dislocation density with cyclic loading during the initial few cycles, which causes the primary cyclic hardening. Rearrangement of dislocation and formation of dislocation walls due to secondary slip activation with increase in the number of cycles causes cyclic softening [177]. Deformation-induced martensitic transformation in 316L strongly depends on strain and strain rate [31]. In this investigation, all the LCF tests were conducted at 0.25 Hz constant frequency. Strain rate, strain amplitude and frequency of cyclic loading in fully reversed conditions can be related as shown in **Eq. 3.2**.

Strain rate = $4 \times$ strain amplitude $\times$ frequency $\hspace{4cm}$ (3.2)

Strain rate becomes equal to strain amplitude at 0.25 Hz frequency and there is an increase in strain rate with increase in strain amplitude. The number of cycles corresponding to the maximum primary hardening, decreases with strain amplitude due to increased dislocation activity with strain rate [148]. The primary cyclic hardening is related to the enhanced dislocation density, whereas secondary hardening may be due to the martensitic transformation induced by deformation [178]. Secondary cyclic hardening was not observed for the HNS, which may be due to its stable microstructure.

The deformation-induced martensitic transformation was absent in high nitrogen-containing stainless steel even after 50% reduction in thickness [166].

The Coffin-Manson (C-M) plots show single slope behavior for the HNS and 316L stainless steels. This observation for the HNS is quite different from the dual-slope observed earlier in the Fe-18Cr-18Mn-0.63N steel [104]. The disparity in the slope of C-M plots in the present and earlier investigations may be due to the difference in the lowest total strain amplitudes in the two studies. While the lowest value of $\Delta\varepsilon_t/2$ was $\pm0.30\%$ in the previous investigation, it is $\pm0.40\%$ in the present study. Therefore, there would have been an activation of mostly single slip system at $\Delta\varepsilon_t/2 = \pm0.30\%$ in the earlier investigation; hence fatigue life was much lower due to early crack initiation in the earlier investigation [104].

Endurance limit of the HNS was found 475 MPa, in which nitrogen content is 0.65%. Park et al. [106] observed 475 MPa endurance limit for 0.59 % nitrogen content in Cr-Mn-N based stainless steel, similar to the HNS. There is a distinct difference in the high cycle fatigue behavior of the HNS and 316L at lower and higher stress levels. It is clear from the tensile test result that the 316L has a very high work hardening rate compared to the HNS and there is deformation-induced martensitic transformation in the 316L. From the engineering stress-strain diagram, it may be seen clearly that about 20% strain is needed to reach the stress level (≤ 525 MPa) due to significant work hardening. A gross elongation of ~ 25 % was observed after fatigue testing and the deformation was mostly during the initial few cycles. It was due to the ratcheting effect as the tests were carried out at R=0.1 and there was a tensile mean stress effect. This gross plastic deformation during the initial few cycles enhanced the strength of the material due to work hardening and fatigue life was high. The HNS has yield strength of 525 MPa and for stress level $\leq$ 525 MPa, it does not experience significant work hardening. At higher stress levels ($\geq$ 538 MPa), with considerable work hardening, there is appreciable amount of formation

of deformation-induced martensite in the 316L. At the interface of austenite and martensite, cracks can easily form and fatigue life is lower at higher stress level. In contrast, no such martensitic transformation was there in the HNS. Also, the damage was significantly less as it was near the YS for the HNS.

3.6.3. Biocompatibility

HNS did not show adverse effects on cell growth, indicating the potential biocompatibility of this stainless steel. Ma et al. [120] studied cytocompatibility of the high nitrogen nickel-free stainless steel with different nitrogen content and found higher cell growth than on the 317L stainless steel. In another study, Li et al. [122] observed that MC3T3-E1 cells adhered well on the high nitrogen stainless steels and the number of attached cells was higher than that on the nitinol alloy. It showed no significant toxic side effects as compared to nitinol alloy for the MC3T3-E1 cells. Thus, the results of this study suggest that the HNS does not cause any toxic effect.

In the present work, the *in vivo* performance of the HNS was also assessed and was found highly promising. The present study demonstrates a normal healing process on gross examination, histopathologically as well radiologically. A progressive decrease in inflammatory response was observed, around the implanted HNS wire, with an increase in the duration of implantation. However, the formation of bony trabeculae along the implant and its thickness increased with the duration of implantation from three weeks to six weeks. *In vitro* study performed by Montaro et al. revealed that P558 (Fe-17Cr-10Mn-3Mo-N, nickel-free stainless steel) was found devoid of mutagenicity and genotoxicity, and considered better than the conventional stainless steel [179,180]. *In vivo* (sheep tibia diaphysis) and *in vitro* study on osteoblast cells using P558 alloy demonstrated a significant increase in osteoblastic differentiation as confirmed by osteocalcin levels, alkaline phosphatase activity and decreased IL-6 level. It was also shown that bone to implant contact (at 26 weeks) was higher in P558 than Ti-6Al-4V and

concluded good biocompatibility of the P558 [118,181]. The absence of nickel might be the probable cause of its excellent biocompatibility. Our study also demonstrated a normal healing process on gross examination, histopathologically as well radiologically. Soft tissue response to P558, Ti6Al4V, ISO 5832-9 was also evaluated by Fini et al. [181]. It demonstrated a higher inflammatory response, capsular thickness in stainless steel ISO5832-9 (Nickel content 9.8 wt%) in rabbit muscle and rat subcutis, while a progressive decrease in the inflammatory response and capsular thickness was seen around the P558 (<0.02% Nickel). In our study, soft tissue response to HNS was found quite similar to the study conducted by Fini et al. [181].

3.7. Conclusions

A nickel-free grade of austenitic stainless steel with negligible nickel (HNS), based on the CrMnN system, was characterized for the microstructure, mechanical properties, corrosion, fatigue and biocompatibility and compared with these properties of the 316L. It has an austenitic microstructure, free from precipitates at the grain boundaries. The HNS was found superior to 316L in mechanical properties like YS and UTS with adequate ductility. Its pitting resistance was found inferior to that of the 316L due to presence of high amount of Mn. Its endurance limit corresponding to 10^7 cycles was lower than that of 316L. The *in vitro* biocompatibility study shows that the HNS did not cause cell growth inhibition and was found comparable to that of the 316L. The *in vivo* biocompatibility study of the HNS confirmed that it did not cause any inflammation and toxic effect in contact with tissues and it is biocompatible. Overall, with negligible nickel, this HNS austenitic stainless steel was found to be better than 316L in terms of tensile properties and has adequate biocompatibility. However, the pitting resistance confirmed by the potentiodynamic polarization study, and the endurance limit are inferior to that of the 316L.